

pubs.acs.org/journal/apchd5 Article

Dual Band Computational Infrared Spectroscopy via Large Aperture Meta-Optics

Johannes E. Fröch, Shane Colburn, Alan Zhan, Zheyi Han, Zhuoran Fang, Abhi Saxena, Luocheng Huang, Karl F. Böhringer, and Arka Majumdar*



Cite This: https://doi.org/10.1021/acsphotonics.2c01017



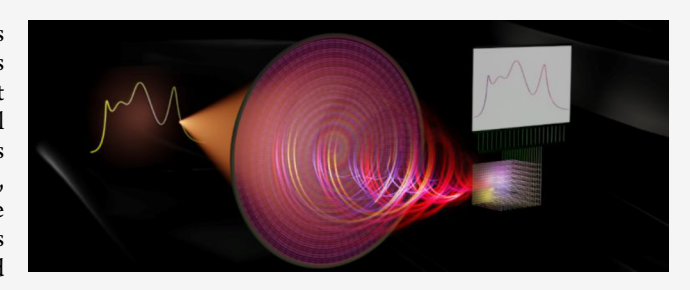
ACCESS I

III Metrics & More

Article Recommendations

s Supporting Information

ABSTRACT: An important challenge in contemporary photonics research is the miniaturization of optical components and devices to facilitate their deployment in more compact and energy-efficient mobile platforms. As spectrometers are one of the most essential tools for optical measurements, a particularly strong demand exists to find new concepts to replace commonly used spectrometers, which are typically bulky and therefore often impractical for mobile applications. Arrays of subwavelength scatterers, also known as meta-optics, engineered to shape and manipulate transmitted optical wavefronts provide a particularly appealing solution for this



problem. Herein, the concept of a computational spectrometer is presented where strongly chromatic point spread functions of a high-efficiency double helix meta-optic are utilized in combination with a computational back end to accurately reconstruct optical spectra. This is demonstrated in two different infrared wavelength ranges (1260-1360 nm and 1480-1640 nm), while achieving a spectral resolution of ~ 3.5 nm, underlining the potential of a small footprint meta-optical spectrometer.

KEYWORDS: dielectric metasurface, computational spectrometer, wavefront coding, computational reconstruction, spectrometer miniaturization

■ INTRODUCTION

The integration of miniaturized spectrometers within mobile devices is becoming increasingly relevant for a plethora of applications, including distributed remote sensing, point-ofcare medical sensors, and personal food monitoring. 1-5 At the same time, design principles for these mobile devices dictate a continuous reduction in size, weight, and power, as these directly affect their ubiquitous deployability. Unfortunately, conventional spectrometers are bulky and impractical as a solution for many of these scenarios. Galvanized by this challenging and important task, several strategies are currently under consideration to overcome the limitations of traditional instruments. An important factor is to maintain a reasonable spectral resolution, for instance by utilizing spectral filters, 6-10 resonant nanowires, 11,12 spectrally dependent photocurrents in nanojunctions, ^{13,14} spectrally dependent point spread functions in scattering media ^{15,16} or diffractive optics. ¹⁷ In many of these approaches, the underlying idea is to exploit a physical system, whose response is wavelength-dependent and thus encodes the spectral information on the captured light into a measurable quantity, which is subsequently decoded using computational techniques.

In recent years, diffractive meta-optics have emerged with compelling potential to drastically reduce the size of optical components, thus addressing the general demand for decreases in size, weight, and power. A meta-optic can shape the optical wavefront with subwavelength spatial resolution via mapping the locally imparted phase shift of each scatterer to a specified phase profile. Going beyond phase control, meta-optics can manipulate other properties of light, including polarization, spectral response, 20–23 spin, and orbital angular momentum. This is particularly appealing for applications that either require multimodal functionalities or cannot be realized using traditional optics. Unsurprisingly, meta-optics have also been used to realize miniaturized spectrometers, for instance using multiple reflective meta-optics in a folded configuration, 28 exploiting the strong chromaticity of a tilted metalens, 29 or using an array of metalenses combined with optical filters. 30

In this work, we combine the capabilities of spectral control via meta-optics and computational postprocessing to demonstrate a computational spectrometer, schematically illustrated in Figure 1. Light from a source with unknown spectrum transmits through a meta-optic, focusing and encoding the spectral distribution into a distinct spatial intensity profile that

Special Issue: Optimized Photonics and Inverse

Design

Received: July 2, 2022



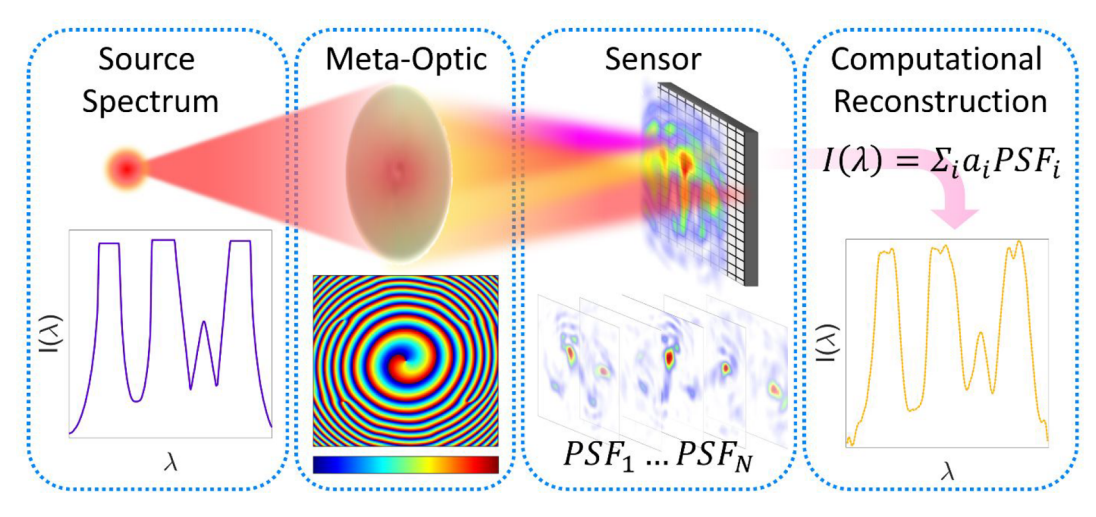


Figure 1. Schematic of the meta-optic computational spectrometer. A meta-optic with a strongly chromatic point spread function defined by a specialized phase mask focuses light of a source spectrum onto a sensor. The source spectral distribution is encoded in the intensity profile, which is captured as an image. The spectrum can then be reconstructed using deconvolution with the knowledge of the wavelength-dependent PSF.

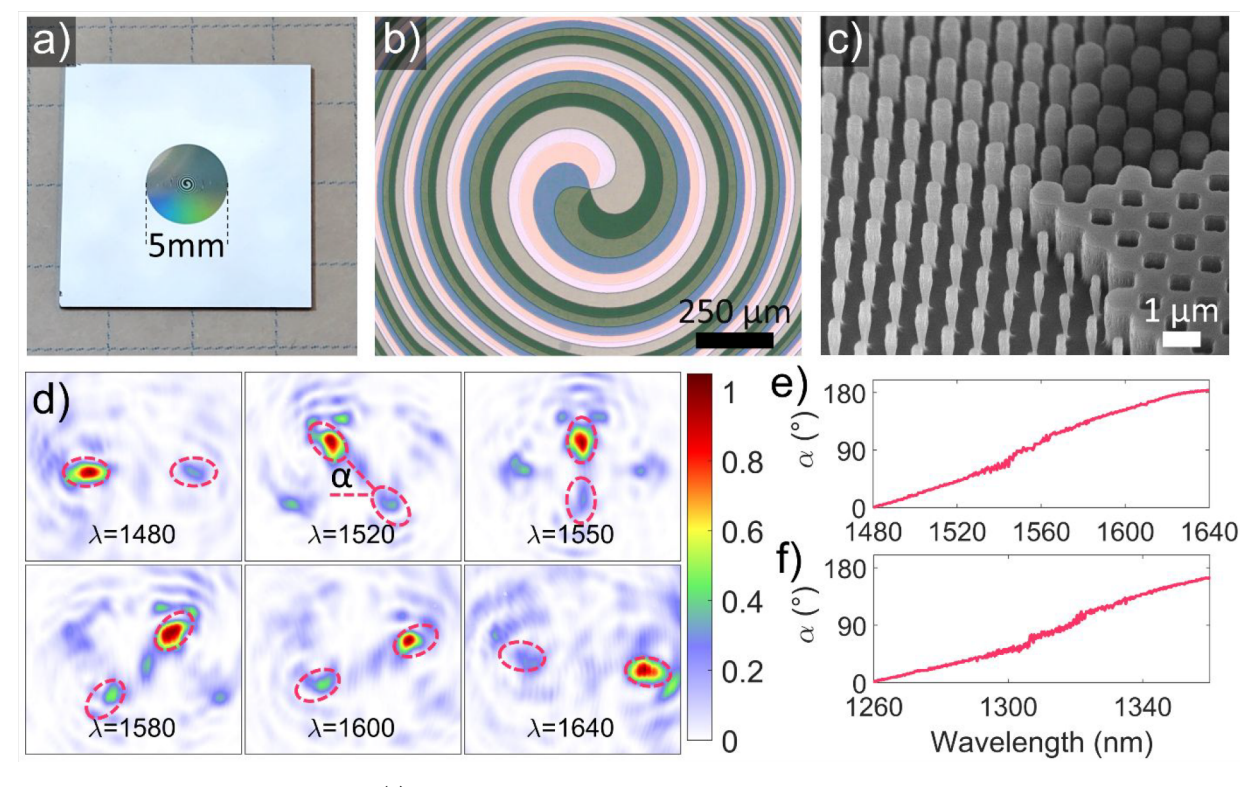


Figure 2. Characterization of the meta-optic. (a) Photograph of the meta-optic chip, placed on graph paper with a 5 mm spacing. The aperture of the meta-optic is 5 mm. (b) Optical microscope image of the fabricated metalens center. (c) SEM image of the device center showing the integrity of the scatterers, taken at an oblique angle of 45°. (d) Point spread functions for various wavelengths in the 1560 nm calibration range. The main lobes are indicated by red dashed circles. Rotation angle of the lobe orientation as a function of wavelength for the 1560 and 1310 nm range are shown in (e) and (f), respectively. A corresponding subset of PSF for the 1310 nm range is presented in the Supporting Information 5.

is then captured using an image sensor. Subsequently, a computational back end decodes the source spectrum using a precalibrated data set of point spread functions (PSFs). Importantly, the meta-optics utilized for this concept must produce unique and spatially separated PSFs to truthfully reconstruct the spectrum. For this purpose, we utilize a meta-optic with a double-helix PSF (DH-PSF),³¹ which we have used in a prior work for depth imaging (further details included in Supporting Information 1).³² While the DH-PSF optics based on refractive elements are generally achromatic and

exhibit a PSF that rotates with defocus, the chromaticity emerges by combining its phase with that of a chromatic hyperboloid metalens. Although a large body of work has focused on mitigating metalens chromatic aberrations, including dispersion engineering ^{33,34} and computational imaging, ^{35,36} we leverage this otherwise unwanted chromaticity in our work to create a spectrometer. Combining the DH-PSF and hyperbolic metalens in a single meta-optic, we create a PSF with two characteristic focused lobes of high intensity rotating with a change in wavelength. Hence, PSFs at

individual wavelengths are unique within the calibration range and have spatial distributions of similar intensities, which facilitates spectral reconstruction. More importantly, by adjusting the focal distance between meta-optic and sensor, we can calibrate the spectrometer to operate in another wavelength range. Generally, the intensity profile produced by a specific source spectrum can be seen as a linear combination of individual PSFs, defined in eq 1,

$$Ax = b \tag{1}$$

where A is the PSF basis set, x is the spectral intensity distribution, and b is the resulting image. Under ideal conditions, this inverse problem can be solved using a least-squares method. In reality, however, the system is ill conditioned, as small perturbations such as experimental noise, or minor drift/vibrations in the measurement setup result in a significant change of the reconstructed spectrum. A common way to tackle such a problem is using Tikhonov regularization (TR), where the term defined in eq 2 is minimized,

$$||Ax = b||^2 + ||\Gamma x||^2 \tag{2}$$

Here $\| \|$ denotes the 2-norm and Γ is the Tikhonov matrix. This approach is more robust to noise and thus drastically improves the stability of the solution, which facilitates spectral reconstruction and enables us to computationally retrieve spectra from experimentally captured intensity profiles.

RESULTS AND DISCUSSION

To demonstrate this concept, we fabricated the dielectric metaoptic in silicon nitride on a silicon substrate with an aperture of 5 mm, focal length of 4 cm, with a central wavelength of 1550 nm. First, the transmission coefficients of the used cylindrical nanoposts were calculated using rigorous coupled-wave analysis, assuming a pillar height of 2 μm and periodicity of 1300 nm, further discussed in Supporting Information 2. The diameter-dependent response was discretized into six levels and mapped to the optimized phase profile, which was then fabricated using high-throughput stepper photolithography (detailed in the Methods) yielding a meta-optic with large apertures of 5 mm, as shown in a photograph in Figure 2a. An optical microscope image of the metalens is shown in Figure 2b, where color variations arise due to a structural color effect that directly mirrors the six-level discretized phase profile. Further details and individual elements can be seen in an oblique angle scanning electron microscope image, shown in Figure 2c, showing the integrity and successful fabrication of the designed pillars.

We then collected the basis set of the meta-optical spectrometer by capturing PSFs for discrete wavelengths over a defined spectral range using a custom microscope relay setup, which consisted of an objective, tube lens, and CCD camera (further illustrated in the Supporting Information 3). Specifically, we used the light from a tunable laser source (Santec TSL-710 or TSL 510A or) with narrow line width to measure PSFs for discrete wavelength values (step size of 0.4 nm) within the spectral range of 1480–1640 nm (and 1260–1360 nm in a second experiment with an adjusted focal distance but the same meta-optic), forming the basis set (i.e., *A* in eq 1) facilitating the computational reconstruction. A subset of the captured PSFs for the 1560 nm range is shown in Figure 2d and a subset for the 1310 nm range is further discussed in Supporting Information 4. As per design, we observed clearly

changing intensity profiles for different wavelengths, exhibiting two characteristic lobes rotating around a common center of gravity, showing a nearly linear dependence of the relative angle with the wavelength, depicted in Figure 2d.

An important condition for the functionality of the presented meta-optic spectrometer is the characteristic wavelength dependence of the PSF, as shown in Figure 2e,f, for the 1560 and 1310 nm range, respectively. This clearly distinguishes the device from other meta-optics, such as a common metalens with a hyperbolic phase profile in two aspects. First, the lobes maintain comparable intensity and shape across the calibration range, in contrast to the diverging PSF of a standard metalens. This is relevant as a lower signalto-noise ratio degrades the quality of the reconstructed spectrum. Second, the PSF for each wavelength is distinct, while other metalens designs exhibit the same change for shorter or longer wavelengths around the design wavelength. This advantage that the DH-PSF exhibits relative to a traditional metalens can also be quantified in terms of Fisher information, where the DH-PSF has been shown to produce a PSF with much higher Fisher information than a standard metalens.³² The range of rotation for the PSF is also the main limiting factor limiting factor for the spectral range. If the rotation angle wraps around π , then the reconstruction becomes less accurate as the PSFs for different wavelengths overlap. However, the spectral range can be extended for example using a multiple aperture system, whereas each aperture covers a specific range. Beyond that simple extension, the design can be further optimized using end-to-end design approach considering a larger wavelength range.

We note that in the simulation (Supporting Information 5), both rotating lobes display the same intensity, while we observed in the experiment that one of the lobes would have significantly higher intensity. We attribute this to an inconsequential misalignment of the optical setup, which does not further impede the operation of the device.

We then assessed the capability of the meta-optical spectrometer to reconstruct spectra from captured intensity profiles. For this purpose, we generated distinct spectral distributions by dispersing the light of a superluminescent diode (SLD - Thorlabs S5FC1550P-A2) from a reflective nearinfrared grating, which was then coupled into a single-mode fiber using an achromatic lens. The light was guided to the meta-optical spectrometer and a conventional spectrometer for direct comparison of the measured spectra. By adjusting the angle of the grating relative to the fiber coupler, we could control the position and width of the spectral distribution. We then used a least-squares method with a non-negative constraint and Tikhonov Regularization with the precalibrated PSFs as the basis set to reconstruct the corresponding spectra. For evaluation, we used Tikhonov matrices of zeroth, first, and second order. While a zeroth order Tikhonov matrix is equivalent to a unity matrix multiplied by a constant, a first and second order matrix include off-diagonal terms, which impose certain constraints in the reconstruction. The reconstructed spectra from these images are shown in comparison to measurements with a grating-based spectrometer (Princeton Instruments) for the 1560 nm range in Figure 3a. The corresponding intensity profiles are exemplarily shown as insets. Further examples of reconstructed spectra for the 1310 range are presented in the Supporting Information 6. Importantly, we demonstrate that throughout the calibrated range, peaks and spectral distributions can be retrieved through

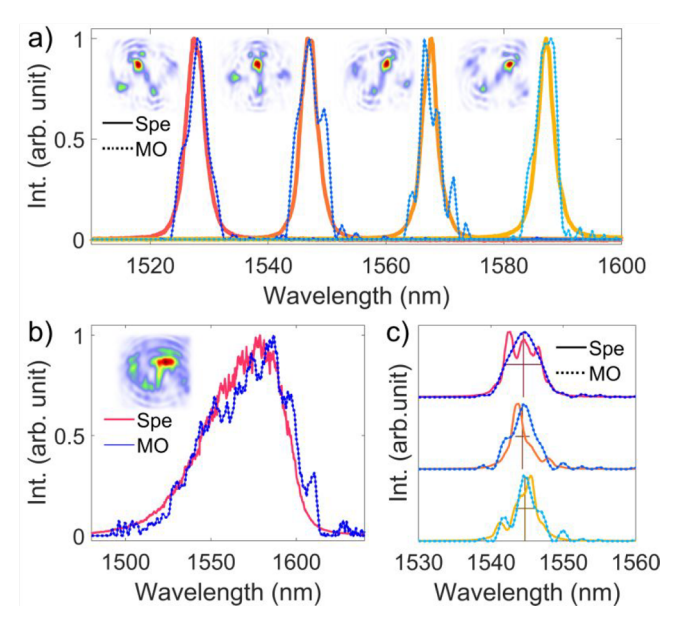


Figure 3. Direct comparison of reconstructed spectra. (a) Reconstructed spectra of the meta-optics (MO) in comparison to measurements with a spectrometer (Spe) for source spectra in a range 1500–1600 nm. The insets correspond to the corresponding captured intensity profiles. (b) Comparison of measured spectrum to reconstructed spectrum of an intensity profile (inset) produced by a SLD with a central wavelength of ~1570 nm. (c) Comparison of measured (Spe) and reconstructed (MO) spectra with small variation and decreasing width of the spectral shape. The spectral centroid and fwhm of the measured spectra are indicated by horizontal and vertical lines.

the reconstruction algorithm, while deviations from the true spectral shape remain small. For an objective assessment, we calculated the root-mean-square error (RMSE) of all spectra, which is 0.04, 0.06, 0.05, and 0.05, for the spectra from left to right, respectively, indicating a consistent accuracy in the reconstruction.

In addition, we retrieved the spectrum from the unfiltered SLD with a broad spectral distribution, which displayed a more dispersed intensity profile, shown in Figure 3b. Similar to the other reconstructed spectra, we obtained a match of the spectral distribution with a RMSE of 0.09, which is of a consistent magnitude as the other presented reconstructed spectra.

To estimate the limitations of the reconstruction process, we

prepared spectral distributions with a decreasing width and varying features. First, a comparison for spectra, prepared by the aforementioned method, was measured and reconstructed, as shown in Figure 3c. The spectral centroid and the fwhm are indicated as vertical and horizontal dashed lines, respectively, whereas the spectral centroid was defined as $\frac{\Sigma \lambda_i I_i}{\Sigma I_i}$, with λ_i as the wavelength at data point i and I_i , the measured intensity value at that wavelength λ_i . For all three presented spectra, the maximum of the reconstructed spectrum closely matches the centroid of the experimentally measured spectrum within the basis set resolution of the computational reconstruction (± 0.2 nm). However, the fwhm is clearly more limited as shown for instance in the reconstructed width of the middle spectrum, which is ~3.5 nm versus the measured width of ~2 nm. Moreover, as the fwhm is limited, certain spectral features such as the three neighboring peaks in the top spectrum are lost in the reconstruction, resulting in a higher error in the reconstruction. At the same time, some features, which are separate on the order of ~5 nm, can be resolved, such as the left shoulder peak in the bottom spectrum.

We note that for the reconstruction of the spectra shown in Figure 3a, we used a second order, while for the spectrum in Figure 3b, a first order Tikhonov Regularization was used, as these achieved a closer match (smaller RMSE) in the reconstruction. The fact that different order matrices can achieve better reconstruction for different spectra is related to the properties of the regularization matrix, which either favor solutions that are broadly smooth (first order Tikhonov matrix) or ones with steeper features. For reconstruction of

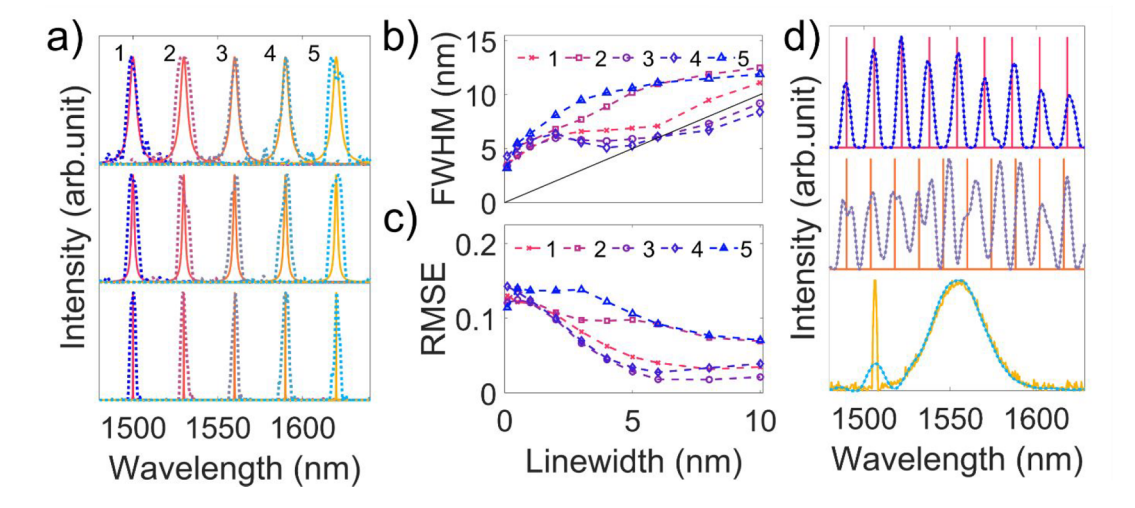


Figure 4. Limitations of computational reconstruction. (a) Examples of reconstructed spectra from synthetic Lorentzian spectra. The line width of the Lorentzian line-shapes from top to bottom is 5, 2, and 0.1 nm. Solid lines indicate the synthetic spectra, dashed lines indicate the reconstructed spectra. 1–5 refer to the peak positions at 1490, 1530, 1560, 1590, and 1620 nm, respectively. (b) and (c) show the fwhm of the reconstructed spectra and the RMSE, respectively. The solid black line in (b) represents the ideal 1:1 relation synthetic line width and reconstructed fwhm. (c) Complex spectral distributions, including frequency combs with decreasing free spectral ranges of 14 nm (top) and 16 nm (middle), as well as a spectrum consisting of broad and sharp features (bottom). Reconstructed spectra are presented as dotted lines.

unknown spectra, an evaluation of the spectral reconstruction would have to be further implemented to choose the order and the value of the constant parameter, such as L-curve or generalized cross validation (GCV).

To further evaluate the resolving capabilities of our spectrometer, we created synthetic spectra using linear combinations of PSFs (step size of 0.1 nm) from the same tunable laser source that was used to create the reconstruction basis set (with a step size of 0.4 nm). These PSFs, however, were not included in the reconstruction basis and therefore represent sums of independent measurements. We first consider the resolution limit of the computational spectrometer, represented by the minimal achievable fwhm retrieved from a single Lorentzian-shaped spectrum. Specifically, we prepared synthetic spectra with decreasing line widths from 10 to 0.1 nm at central wavelengths of 1500, 1530, 1560, 1590, and 1620 nm, of which a subset (5, 2, and 0.1 nm) is shown in Figure 4a. Consistent with measured spectra (Figure 3c), we observe that the centroid is closely matched, typically within ± 0.2 nm. From the reconstructed spectra we extracted the fwhm and RMSE, shown in Figure 4b and c, respectively, whereas the numbering 1-5 refers to their central wavelength of 1500, 1530, 1560, 1590, and 1620 nm, respectively. For a Lorentzian line width of 0.1 nm, we retrieved an average value for the resolution of \sim 3.5 nm. Within a range of 0.1 nm to \sim 2 nm for the synthetic line width, we observe a linear increase in fwhm of the reconstructed spectra, followed by a plateau up to ~5 nm and then a linear increase of the fwhm, closely matching the synthetic line width above 5 nm. At the same time, the RMSE follows similar trends, indicating high discrepancies in the reconstruction of smaller line widths with an RMSE of ~0.12 at the limit, which decreases and then plateaus to 0.04 for line widths of 10 nm. We note that the reconstruction for spectra centered at 1530 and 1620 nm show worse performance in comparison to others, which may indicate limitations for the approach of using synthetic spectra. One reason could be that, as PSFs are captured at discrete values, certain features in the intensity profile of the synthetic spectrum are not fully represented, thus slightly impeding the reconstruction. Evidence for this interpretation can also be seen in the reconstructed spectra in Figure 4a, which indicate the reconstruction of two neighboring lines instead of one continuous spectral distribution, thus leading to a broadening of the fwhm in the reconstructed spectra.

As a further limitation of the reconstruction, we consider more complex spectra than single lines, such as with a higher density of single frequency lines. As demonstrated in Figure 4d, this clearly hampers the reconstruction. Specifically, we prepared combs of single frequency lines with decreasing free spectral range (FSR) and found that for an FSR of 16 nm, the centroids and number of peaks can be accurately reconstructed, although with a higher fwhm as compared to single isolated lines (Figure 4a); however, as the FSR decreases to 14 nm, reconstruction artifacts appear and the number and centroids of the frequency comb are only roughly matched.

Another limitation of the Tikhonov Regularization-based reconstruction arises for spectral distributions containing mixed narrow and broad features (bottom, Figure 4d). Simultaneous reconstruction of both feature types with the same regularization parameter and order becomes unattainable, as can be clearly seen at a narrow peak in the spectrum. This is related to the characteristics of the Tikhonov Regularization, where through its order and regularization

parameter certain constraints are imposed. Nevertheless, we note that although the sharper peak in the spectrum does appear with a significantly broader fwhm in the reconstruction than other cases in Figure 4, the central frequency could still be accurately retrieved.

While the spectral reconstruction in the presented concept is limited by the computational back end, we believe that the performance can be significantly improved by using a machine learning approach to improve the computational reconstruction³⁷ and by employing a co-optimization of the meta-optics front end and the computational backend, which has previously been employed for full color imaging³⁶ and proposed as a potential solution for a diverse range of functionalities.^{38,39} Such an inverse end-to-end design approach could further improve the spectral range of the spectrometer and help to improve the spectral resolution.

CONCLUSION

In summary, we have demonstrated the concept of a metaoptics computational spectrometer consisting of a meta-optical frontend which encodes the spectral distribution of a light source into a distinct intensity profile, which is captured with a sensor and subsequently decoded using a computational back end, using a precalibrated data set of PSFs in the given wavelength ranges. The unique properties of the meta-optic arise from combining the characteristic chromaticity of a metalens with a high-efficiency rotating double-helix PSF. This specific concept is demonstrated for two spectral ranges in the infrared wavelength range, from 1260-1360 nm and 1480-1640 nm. We demonstrate accurate reconstruction of various spectra and achieve a spectral resolution of ~3.5 nm, which is on par with other works using computational spectrometers. Beyond the capabilities as a spectrometer, we believe that the true benefit of the meta-optic will be fully leveraged once it is combined with a second metalens for image reconstruction. We have previously demonstrated a similar concept, where a dual-aperture arrangement was used for image reconstruction in a depth imaging system. A similar approach can create a platform for hyperspectral imaging with a compact footprint that would be appealing for integration within mobile devices.

METHODS

Device Fabrication. The silicon nitride meta-optics were fabricated on a 525 μ m thick double side polished silicon wafer, lightly doped with boron, giving a sheet resistivity of 8-15 Ω ·cm. We deposited a 2 μ m thick silicon nitride layer with a plasma-enhanced chemical vapor deposition (PECVD) at 350 °C (SPTS SPM). We utilized stepper lithography (Canon FPA-3000 i4) to pattern the meta-optics in the photoresist layer. A 170 nm thick aluminum layer was evaporated (CHA Solution) and lifted off to create a hard mask for etching. Then we transferred the pattern to the 2 μ m silicon nitride layer via fluorine-based inductively coupled plasma (ICP) etching (Oxford PlasmaLab 100). The residual aluminum hard mask was stripped in an aqueous solution containing 2.38% tetramethylammonium hydroxide (TMAH). The cleaned wafer was then diced (Disco DAD321) into individual chips carrying one meta-optic each for optical experiments.

Optical Setup. For all calibration and spectral measurements, we used a setup consisting of an objective (40×), tube lens, and NIR CCD camera (Pembroke WiDy SenS 320). The meta-optics was placed in front of the objective. Light for

calibration or measurement of the meta-optics was launched from a single-mode fiber and collimated using an achromatic doublet lens (Thorlabs AC 254-C). We calibrated the metaoptics spectrometer by measuring the generated PSF from a tunable laser. For these measurements, the output of a fibercoupled tunable laser source (Santec TSL-510A for 1310 nm range and TSL-710 for 1550 nm range) was connected to the single-mode fiber leading to the meta-optics spectrometer. The laser was tuned to a wavelength either in a spectral range of 1260-1360 nm or 1480-1640 nm. For these subsequent measurements the distance of the meta-optics relative to the objective was adjusted, that is, refocusing such that either the PSF of 1310 or 1560 nm was at the central focal length. For calibration, we captured 30 frames with a 2 ms integration time, which were averaged to minimize the contribution of noise to the image. Further, we subtracted the sensor and setup background from all PSF measurements, for which 100 frames were captured with no laser illumination. For the measurement of the SLD spectrum (discussed in Figure 3), we connected another fiber to the output of the light source, which was connected either to the fiber leading to the meta-optics spectrometer or a grating-based spectrometer (Princeton Instruments SP-2750, PyLoN-IR). Other spectral shapes discussed in Figure 3 and Supporting Information 6 were generated by guiding the light of the SLD through a fiber to a grating, which dispersed it spectrally.

ASSOCIATED CONTENT

5 Supporting Information

The Supporting Information is available free of charge at https://pubs.acs.org/doi/10.1021/acsphotonics.2c01017.

Design of phase mask, scatterer design, measurement setup, PSFs for the 1330 nm range, computed intensity profiles, and reconstructed spectra in the 1310 nm range (PDF)

AUTHOR INFORMATION

Corresponding Author

Arka Majumdar — Department of Physics and Department of Electrical and Computer Engineering, University of Washington, Seattle, Washington 98195, United States;
orcid.org/0000-0003-0917-590X; Email: arka@uw.edu

Authors

Johannes E. Fröch – Department of Physics and Department of Electrical and Computer Engineering, University of Washington, Seattle, Washington 98195, United States

Shane Colburn – Department of Electrical and Computer Engineering, University of Washington, Seattle, Washington 98195, United States; Tunoptix, Seattle, Washington 98195, United States

Alan Zhan – Tunoptix, Seattle, Washington 98195, United States

Zheyi Han — Department of Electrical and Computer Engineering, University of Washington, Seattle, Washington 98195, United States

Zhuoran Fang — Department of Electrical and Computer Engineering, University of Washington, Seattle, Washington 98195, United States; ⊚ orcid.org/0000-0001-8724-6633

Abhi Saxena — Department of Electrical and Computer Engineering, University of Washington, Seattle, Washington 98195, United States; orcid.org/0000-0001-6453-929X

Luocheng Huang — Department of Electrical and Computer Engineering, University of Washington, Seattle, Washington 98195, United States

Karl F. Böhringer — Department of Electrical and Computer Engineering, Department of Bioengineering, and Institute for Nano-Engineered Systems, University of Washington, Seattle, Washington 98195, United States; orcid.org/0000-0002-9428-2648

Complete contact information is available at: https://pubs.acs.org/10.1021/acsphotonics.2c01017

Funding

This research was funded by NSF-1825308, NSF-2127235, NSF-GCR-2120774, and NASA (Contract No. 80NSSC21C0419). A.M. is also supported by the Washington Research Foundation.

Notes

The authors declare the following competing financial interest(s): A.Z., S.C., K.B., and A.M. are part of Tunoptix, a company trying to commercialize this technology.

ACKNOWLEDGMENTS

Part of this work was conducted at the Washington Nanofabrication Facility/Molecular Analysis Facility, a National Nanotechnology Coordinated Infrastructure (NNCI) site at the University of Washington, with partial support from the National Science Foundation via Awards NNCI-1542101 and NNCI-2025489.

REFERENCES

- (1) Mouroulis, P.; Green, R. O. Review of High Fidelity Imaging Spectrometer Design for Remote Sensing. *Opt. Eng.* **2018**, *57* (4), 040901.
- (2) Yang, Z.; Albrow-Owen, T.; Cai, W.; Hasan, T. Miniaturization of Optical Spectrometers. *Science* **2021**, *371* (6528), No. eabe0722.
- (3) Bastawrous, A.; Rono, H. K.; Livingstone, I. A. T.; Weiss, H. A.; Jordan, S.; Kuper, H.; Burton, M. J. Development and Validation of a Smartphone-Based Visual Acuity Test (Peek Acuity) for Clinical Practice and Community-Based Fieldwork. *JAMA Ophthalmology* **2015**, 133 (8), 930–937.
- (4) Cruz-Tirado, J. P.; Lucimar da Silva Medeiros, M.; Barbin, D. F. On-Line Monitoring of Egg Freshness Using a Portable NIR Spectrometer in Tandem with Machine Learning. *Journal of Food Engineering* **2021**, 306, 110643.
- (5) McGonigle, A. J. S.; Wilkes, T. C.; Pering, T. D.; Willmott, J. R.; Cook, J. M.; Mims, F. M.; Parisi, A. V. Smartphone Spectrometers. *Sensors* **2018**, *18* (1), 223.
- (6) Kurokawa, U.; Choi, B. I.; Chang, C.-C. Filter-Based Miniature Spectrometers: Spectrum Reconstruction Using Adaptive Regularization. *IEEE Sensors Journal* **2011**, *11* (7), 1556–1563.
- (7) Li, E.; Chong, X.; Ren, F.; Wang, A. X. Broadband On-Chip near-Infrared Spectroscopy Based on a Plasmonic Grating Filter Array. Opt. Lett., OL 2016, 41 (9), 1913–1916.
- (8) Craig, B.; Shrestha, V. R.; Meng, J.; Cadusch, J. J.; Crozier, K. B. Experimental Demonstration of Infrared Spectral Reconstruction Using Plasmonic Metasurfaces. *Opt. Lett., OL* **2018**, 43 (18), 4481–4484.
- (9) Tittl, A.; Leitis, A.; Liu, M.; Yesilkoy, F.; Choi, D.-Y.; Neshev, D. N.; Kivshar, Y. S.; Altug, H. Imaging-Based Molecular Barcoding with Pixelated Dielectric Metasurfaces. *Science* **2018**, *360* (6393), 1105–1109.
- (10) Shrestha, V. R.; Craig, B.; Meng, J.; Bullock, J.; Javey, A.; Crozier, K. B. Mid- to Long-Wave Infrared Computational Spectroscopy with a Graphene Metasurface Modulator. *Sci. Rep* **2020**, *10* (1), 5377.

- (11) Cadusch, J. J.; Meng, J.; Wen, D.; Shrestha, V. R.; Crozier, K. B. Compact, Lightweight, and Filter-Free: An All-Si Microspectrometer Chip for Visible Light Spectroscopy. ACS Photonics 2022, 9 (2), 474-481.
- (12) Meng, J.; Cadusch, J. J.; Crozier, K. B. Detector-Only Spectrometer Based on Structurally Colored Silicon Nanowires and a Reconstruction Algorithm. Nano Lett. 2020, 20 (1), 320-328.
- (13) Yuan, S.; Naveh, D.; Watanabe, K.; Taniguchi, T.; Xia, F. A Wavelength-Scale Black Phosphorus Spectrometer. Nat. Photon 2021, 15 (8), 601–607.
- (14) Yang, Z.; Albrow-Owen, T.; Cui, H.; Alexander-Webber, J.; Gu, F.; Wang, X.; Wu, T.-C.; Zhuge, M.; Williams, C.; Wang, P.; Zayats, A. V.; Cai, W.; Dai, L.; Hofmann, S.; Overend, M.; Tong, L.; Yang, Q.; Sun, Z.; Hasan, T. Single-Nanowire Spectrometers. Science 2019, 365 (6457), 1017–1020.
- (15) Wang, P.; Menon, R. Computational Spectrometer Based on a Broadband Diffractive Optic. Opt. Express, OE 2014, 22 (12), 14575-
- (16) Hartmann, W.; Varytis, P.; Gehring, H.; Walter, N.; Beutel, F.; Busch, K.; Pernice, W. Waveguide-Integrated Broadband Spectrometer Based on Tailored Disorder. Advanced Optical Materials 2020, 8 (6), 1901602.
- (17) Edwards, P.; Zhang, C.; Zhang, B.; Hong, X.; Nagarajan, V. K.; Yu, B.; Liu, Z. Smartphone Based Optical Spectrometer for Diffusive Reflectance Spectroscopic Measurement of Hemoglobin. Sci. Rep 2017, 7 (1), 12224.
- (18) Khorasaninejad, M.; Crozier, K. B. Silicon Nanofin Grating as a Miniature Chirality-Distinguishing Beam-Splitter. Nat. Commun. **2014**, 5 (1), 5386.
- (19) Carletti, L.; Zilli, A.; Moia, F.; Toma, A.; Finazzi, M.; De Angelis, C.; Neshev, D. N.; Celebrano, M. Steering and Encoding the Polarization of the Second Harmonic in the Visible with a Monolithic LiNbO3Metasurface. ACS Photonics 2021, 8 (3), 731-737.
- (20) Park, C.-S.; Shrestha, V. R.; Yue, W.; Gao, S.; Lee, S.-S.; Kim, E.-S.; Choi, D.-Y. Structural Color Filters Enabled by a Dielectric Metasurface Incorporating Hydrogenated Amorphous Silicon Nanodisks. Sci. Rep 2017, 7 (1), 2556.
- (21) Cheng, F.; Gao, J.; Luk, T. S.; Yang, X. Structural Color Printing Based on Plasmonic Metasurfaces of Perfect Light Absorption. Sci. Rep 2015, 5 (1), 11045.
- (22) Yang, W.; Xiao, S.; Song, Q.; Liu, Y.; Wu, Y.; Wang, S.; Yu, J.; Han, J.; Tsai, D.-P. All-Dielectric Metasurface for High-Performance Structural Color. Nat. Commun. 2020, 11 (1), 1864.
- (23) Seo, K.; Wober, M.; Steinvurzel, P.; Schonbrun, E.; Dan, Y.; Ellenbogen, T.; Crozier, K. B. Multicolored Vertical Silicon Nanowires. Nano Lett. 2011, 11 (4), 1851-1856.
- (24) Chong, K. E.; Staude, I.; James, A.; Dominguez, J.; Liu, S.; Campione, S.; Subramania, G. S.; Luk, T. S.; Decker, M.; Neshev, D. N.; Brener, I.; Kivshar, Y. S. Polarization-Independent Silicon Metadevices for Efficient Optical Wavefront Control. Nano Lett. **2015**, 15 (8), 5369-5374.
- (25) Fang, X.; Ren, H.; Gu, M. Orbital Angular Momentum Holography for High-Security Encryption. Nat. Photonics 2020, 14 (2), 102-108.
- (26) Ren, H.; Maier, S. A. Nanophotonic Materials for Twisted-Light Manipulation. Adv. Mater. 2021, n/a (n/a), 2106692.
- (27) Ren, H.; Fang, X.; Jang, J.; Bürger, J.; Rho, J.; Maier, S. A. Complex-Amplitude Metasurface-Based Orbital Angular Momentum Holography in Momentum Space. Nat. Nanotechnol 2020, 15 (11), 948 - 955.
- (28) Faraji-Dana, M.; Arbabi, E.; Arbabi, A.; Kamali, S. M.; Kwon, H.; Faraon, A. Compact Folded Metasurface Spectrometer. Nat. Commun. 2018, 9 (1), 4196.
- (29) Zhu, A. Y.; Chen, W.-T.; Khorasaninejad, M.; Oh, J.; Zaidi, A.; Mishra, I.; Devlin, R. C.; Capasso, F. Ultra-Compact Visible Chiral Spectrometer with Meta-Lenses. APL Photonics 2017, 2 (3), 036103.
- (30) McClung, A.; Samudrala, S.; Torfeh, M.; Mansouree, M.; Arbabi, A. Snapshot Spectral Imaging with Parallel Metasystems. Science Advances 2020, 6 (38), No. eabc7646.

- (31) Pavani, S. R. P.; Piestun, R. High-Efficiency Rotating Point Spread Functions. Opt. Express, OE 2008, 16 (5), 3484-3489.
- (32) Colburn, S.; Majumdar, A. Metasurface Generation of Paired Accelerating and Rotating Optical Beams for Passive Ranging and Scene Reconstruction. ACS Photonics 2020, 7 (6), 1529-1536.
- (33) Chen, W. T.; Zhu, A. Y.; Sanjeev, V.; Khorasaninejad, M.; Shi, Z.; Lee, E.; Capasso, F. A Broadband Achromatic Metalens for Focusing and Imaging in the Visible. Nat. Nanotechnol. 2018, 13 (3), 220 - 226.
- (34) Wang, S.; Wu, P. C.; Su, V.-C.; Lai, Y.-C.; Chen, M.-K.; Kuo, H. Y.; Chen, B. H.; Chen, Y. H.; Huang, T.-T.; Wang, J.-H.; Lin, R.-M.; Kuan, C.-H.; Li, T.; Wang, Z.; Zhu, S.; Tsai, D. P. A Broadband Achromatic Metalens in the Visible. Nat. Nanotechnol. 2018, 13 (3), 227-232.
- (35) Colburn, S.; Zhan, A.; Majumdar, A. Metasurface Optics for Full-Color Computational Imaging. Science Advances 2018, 4 (2), No. eaar2114.
- (36) Tseng, E.; Colburn, S.; Whitehead, J.; Huang, L.; Baek, S.-H.; Majumdar, A.; Heide, F. Neural Nano-Optics for High-Quality Thin Lens Imaging. Nat. Commun. 2021, 12 (1), 6493.
- (37) Gao, L.; Qu, Y.; Wang, L.; Yu, Z. Computational Spectrometers Enabled by Nanophotonics and Deep Learning. Nanophotonics 2022, 11 (11), 2507-2529.
- (38) Lin, Z.; Roques-Carmes, C.; Pestourie, R.; Soljačić, M.; Majumdar, A.; Johnson, S. G. End-to-End Nanophotonic Inverse Design for Imaging and Polarimetry. Nanophotonics 2021, 10 (3), 1177-1187.
- (39) Lin, Z.; Pestourie, R.; Roques-Carmes, C.; Li, Z.; Capasso, F.; Soljačić, M.; Soljačić, M.; Johnson, S. G. End-to-End Metasurface Inverse Design for Single-Shot Multi-Channel Imaging. Opt. Express **2022**, 30 (16), 28358–28370.

□ Recommended by ACS

An All-Dielectric Metasurface Polarimeter

Yash D. Shah, Daniele Faccio, et al.

SEPTEMBER 15, 2022

ACS PHOTONICS

READ **Z**

Ultracompact Orbital Angular Momentum Sorter on a CMOS Chip

Jiaping Cheng, Shumin Xiao, et al.

MAY 05, 2022

NANO LETTERS

READ

Single-Pulse Measurement of Orbital Angular Momentum **Generated by Microring Lasers**

Robert C. Keitel, David J. Norris, et al.

NOVEMBER 15, 2021

ACS NANO

READ 🗹

Generalized Modular Spectrometers Combining a Compact Nanobeam Microcavity and Computational Reconstruction

Ziwei Cheng, Xinliang Zhang, et al.

DECEMBER 14, 2021

ACS PHOTONICS

READ **'**

Get More Suggestions >